Numerical Study of Ammonia Sprays with a GDI Engine Injector

Zembi J[a], Battistoni M[a] [*], Pandal A[b], Rouselle C[c], Pelé R[c], Brequigny P[c], Hespel C[c]

[a]*University of Perugia, Department of Engineering, 06123 Perugia, Italy*
[b]*University of Oviedo, Dpto. Energía, 33202 Gijón (Asturias), Spain*
[c]*University of Orleans, NSA-CVL, EA 4229—PRISME, 45072 Orléans, France*

Abstract

With the aim of expanding the knowledge on liquid ammonia sprays, this paper investigates the injection process of ammonia through Computational Fluid Dynamics (CFD) using the Lagrangian particle method, within the Reynolds Averaged Navier Stokes (RANS) approach for turbulence modeling. Numerical results and experimental data are compared in terms of liquid and vapor tip penetration, local values of Sauter Mean Diameter (SMD) and global spray morphology. This model validation process allows to build a predictive simulation framework for ammonia injection. In order to explore also the flash boiling phenomenon, results of CFD simulations of ammonia spray and the comparison with experimental data are presented for different conditions, ranging from non-flashing regimes to flash boiling conditions. Breakup model constants need to be markedly tuned for each regime, and established values for traditional fuels, like gasoline, appear not to work well with ammonia. Ultimately, this study highlights that capturing spray local details (such as local SMD values) across all the regimes with a single model or setup is still challenging, especially with a new fuel such as ammonia, whose properties differ by a large amount from more established values for hydrocarbons.

Introduction

Nowadays, research in the use of carbon-free energy sources is more and more important in the perspective of climate change mitigation. In this scenario, green hydrogen appears as one of the best options. However, considering the difficulty and high costs associated with its storage, there is growing interest in using ammonia as a fuel for internal combustion engines or gas turbines. Using carbon-free energy sources is key to reduce CO_2 emissions, and large research efforts are directed towards the green revolution for zero-emission mobility and heavy-duty transportation. This process requires a global transition from fossil to renewable energy sources use in the next decades. Hydrogen promises to be one of these carbon free energies [1], but it has dangerous properties such as an extremely low ignition energy and a very wide flammability range [2], and its density is too low to be easily transported and stored safely and economically [3]. Ammonia, an efficient hydrogen carrier, can be directly considered as a fuel for Internal Combustion Engines (ICEs) or gas turbines [4-6], given its high hydrogen content (17.8% hydrogen content by mass) and ease of safe storage [7]. Considering the direct injection scenario in an ICE, pressurized ammonia is in liquid state. The

injection process and spray atomization play an important role on the control of local air/fuel ratio, which affects the combustion development and therefore pollutant emissions [8]. Ammonia is characterized by a vapor pressure curve higher than the vapor pressure of other typical fuels, such as gasoline or ethanol, and flash boiling phenomena might occur in regular operating conditions. However, the phenomena occurring during the vaporization process are difficult to access experimentally, especially for flash boiling conditions. Flash boiling phenomenon happens when a subcooled liquid is injected at high pressure in a low-pressure environment below its saturation pressure [9], producing a faster atomization process, driven by large degree of superheat [10]. In multi-hole nozzles this then causes plume-to-plume collapse and different spray behaviors and morphologies [11]. Two flash boiling regimes can be identified, namely internal and external flashing. The first one is originated inside the injector orifice and the spray turns out to be a two-phase flow composed of liquid and vapor [12]. The second one occurs directly out of the injector orifice with a rapid fuel vaporization [13].

Focusing on combustion engines, an in-depth study of the ammonia injection into the combustion

chamber is necessary, since very few studies on ammonia spray are available in the literature [14-18]. Pelé et al. [14] investigated the ammonia spray characteristics with a seven-hole Gasoline Direct Injector (GDI) injector in different operating situations, from flash boiling to non-flashing conditions. These experimental data provide the first information about ammonia injection with a current spark-ignition GDI injector. Li et al. [15] explored the spray characteristics of ammonia under different fuel temperatures and ambient densities in a constant volume chamber to cover a wide range of superheat degrees. In this study the near-field bubble explosion intensity and the far-field tip penetration evolution characteristics of superheated ammonia spray have been investigated systematically for the first time. Cheng et al. [16] compared ammonia, methanol and ethanol spray behavior in engine-like conditions using high-speed Schlieren imaging technique to capture the spray evolution. Scharl et al. [17] carried out optical investigations and heat release rate analyses complemented by 1-D spray modeling to provide fundamental insight into distinctive features of ammonia spray combustion and mixtures formation under engine-relevant conditions in a rapid-compression-expansion-machine.

From the numerical point of view, Gaucherand et al. [18] and Pandal et al. [19] explored the ammonia spray behavior using CFD simulations. The first study [18] shows RANS simulations of the internal flow of a GDI operating with liquid ammonia, demonstrating that it is indeed possible to adapt an ICE to ammonia fuel with minor changes to the injector design. In the second work [19] direct-injected ammonia spray is modeled with the Lagrangian particle approach, within the OpenFOAM framework for transient analyses, and a comparison between flash boiling and non-flashing regimes is presented and discussed, highlighting challenges due to the new fuel properties.

Numerical studies can complement the macroscopic description of the spray at the microscopic scale. The present study focuses on the numerical simulation of a liquid-ammonia spray and its comparison with experiments by Pelè et al. [14]. An exploration of main spray breakup and phase-change parameters is carried out to build a predictive Lagrangian model for ammonia based on the validation against experimental liquid and vapor tip penetrations, local values of Sauter mean diameter and global spray morphology.

Experimental Setup and Measurements

Experimental imaging data have been presented and discussed extensively in [14], and only a brief description of the available data is reported here for the sake of comprehensiveness. A 2.5 l constant volume chamber is used for experimental measurements where the backpressure can be increased up to 30 bar (by an air compressor) and the ambient temperature warmed-up up to 473 K (by wall heating resistances). Ammonia is pressurized up to 120 bar by means of pressurized Helium. The injector is a current Bosch gasoline direct injector comprised of 7 holes of 150 μm diameter. The temperature and injection duration were controlled. The Schlieren technique was setup to follow the liquid and vapor spray development.
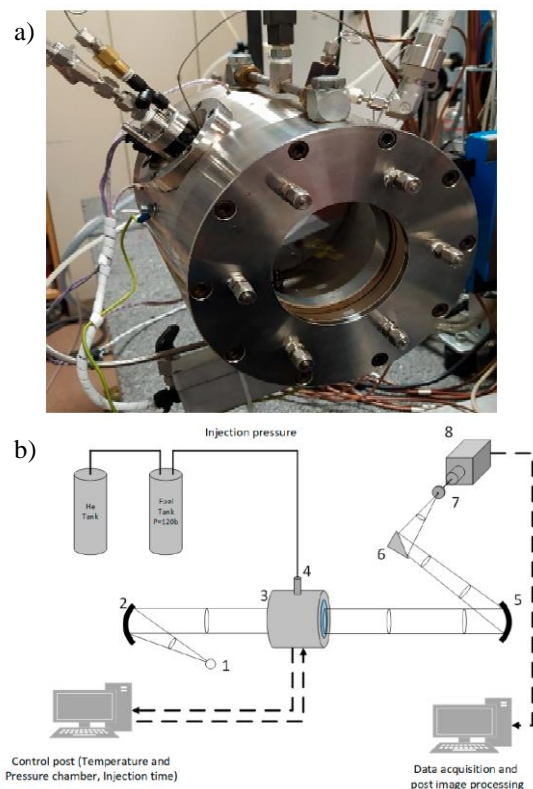

Fig. 1. View of the 2.5 l constant volume chamber with optical accesses (a). Schematics of the experimental and optical setup (b): 1 Light ED source; 2 and 5 Concave mirrors; 3 Chamber; 4 Injector; 6 Plane mirror; 7 Adjustable diaphragm; 8 CMos FastCam (High speed camera).

Post-processing of 100 raw images was performed. The high sensitivity to refractive index gradients makes it possible to identify the limit of the line of sight between the vaporized fuel and the ambient gases [20]. The sensitivity is a function of the light intensity and is adjustable by a diaphragm in front of the camera; a small diaphragm opening increases the sensitivity. A view of the chamber and the scheme of the experimental setup are shown in Fig. 1.

In addition, droplet size measurement with a Malvern Spraytech droplet size analyzer was done at different locations in the spray: in the central point,

and on the spray boundary close and far from the injector nozzle as indicated in Fig. 2.
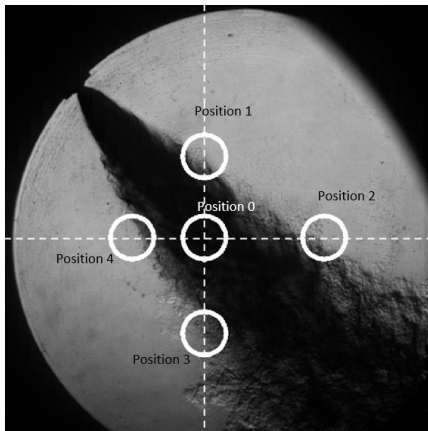

Fig. 2. Example of the position of the measurement of the droplet size distribution for ammonia spray.

In Fig. 3 the ammonia vapor pressure is plotted in comparison to the gasoline vapor pressure. It can be clearly noticed that the two curves are very different, the ammonia curve is higher than the gasoline curve. As an example, at 293 K the ammonia vapor pressure is about 8 bar (8.57 bar) compared to 0.22 bar for gasoline. This fundamental parameter distinguishes two types of regimes. For ambient pressure and fuel injection temperature conditions below the vapor pressure trace, the injection operates under flash boiling conditions while above it is in non-flashing condition. The spray shape, its development and the atomization are completely different between these two regimes. This large change in saturation pressure between ammonia and hydrocarbon fuels causes big challenges for simulations aimed at correctly reproducing experimental behaviors. This study focuses on 7 ammonia injection conditions, with 4 cases nominally falling in the non-flashing regime (points circled in cyan) and 3 in flash boiling regime (points circled in green).

In Table 1, experimental Sauter mean diameter D_{32} (SMD) values in five selected positions are provided as a function of ambient pressures, at the fuel and ambient temperature of 293 K. Interestingly, SMD increases continuously with ambient pressure, without showing two distinct regimes below and above p_{sat}. In the far periphery (points 2 and 3, cf. Fig. 1) larger diameters are found.
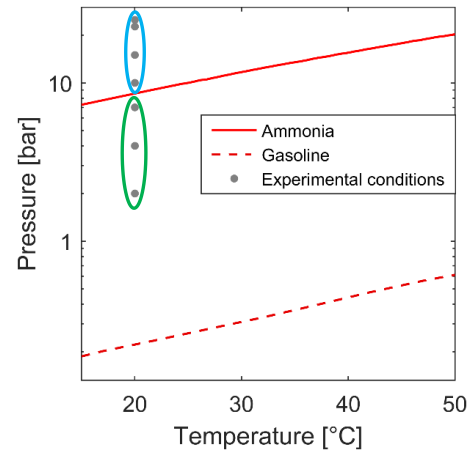

Fig. 3. Comparison between vapor pressure curve of ammonia and gasoline, with experimental tested conditions [8].

Table 1. Experimental SMD [µm] in 5 positions inside the ammonia spray for 5 ambient pressures

	Chamber pressure	2 bar	4 bar	7 bar	10 bar	15 bar
	p_{amb}/p_{sat}	0.25	0.5	0.875	1.25	1.875
Position	0	8.6	14.4	20.4	26.3	33.6
	1	8.5	12.6	17.7	22.2	30.3
	2	12.0	18.5	26.9	31.5	39.2
	3	11.5	17.2	28.6	37.7	48.5
	4	8.4	14.5	15.8	28.2	41.0

Computational Method

A numerical model has been built with the CONVERGE v3.0 CFD software package [21, 22]. Prescribed and adaptive refinements are easily handled with user-controlled parameters. The finite volume method is used to solve the overall set of compressible Favre-averaged equations. Conservation of mass and momentum are solved via a pressure-velocity coupling algorithm, using the Pressure Implicit with Splitting of Operators (PISO) method [23]. In the current study, the accuracy of the numerical schemes used is second-order in space, with flux-limiter, and first order in time. The mesh is generated on-the-fly with an efficient method, based on orthogonal grids with cut-cells at the boundaries. Prescribed and adaptive refinements are easily handled with user-controlled parameters. The mesh base size is 4.0 mm while the finest resolution of 0.25 mm is reached around the injector nozzle; moreover, Adaptive Mesh Refinement (AMR)

techniques based on velocity, temperature and species gradients are used in the spray region to reach a resolution of 0.5 mm.

The computation domain is a cylinder, as shown in Fig. 4.a. Details of the nominal plume geometry and orientation are show in Fig. 4.b. The ammonia spray is modeled with the Lagrangian particle approach [24], paying attention to cell and parcel counts for discretization independent results. The fuel is injected at 120 bar and 293 K. The blob model is used for the injection, the breakup can then occur upon parcels introduction following the competing Kelvin-Helmholtz and Rayleigh-Taylor (KH-RT) models. In the KH model, the initial parcel diameters are set equal to the nozzle hole diameter d_0 reduced by the area contraction coefficient, and the primary atomization process of the relatively large, injected blobs is modeled using the stability analysis for liquid jets. The breakup and resulting drops are calculated by assuming that the detached drop radius r_c is proportional to the wavelength of the fastest growing unstable surface wave Λ_{KH},

$$r_c = B_0 \Lambda_{KH} \tag{1}$$

where B_0 is the KH model size constant. The rate of change of drop radius r_p in a parent parcel is given by,

$$\frac{dr_p}{dt} = -\frac{(r_p - r_c)}{\tau_{KH}} \tag{2}$$

where the breakup time τ_{KH} is calculated including the KH breakup time constant B_1,

$$\tau_{KH} = \frac{3.726 \, B_1 \, r_p}{\Lambda_{KH} \, \Omega_{KH}} \tag{3}$$

In addition to the KH breakup mechanism, the Rayleigh-Taylor instability is also believed to be responsible for droplet breakup. The unstable RT waves are thought to occur due to the rapid deceleration of the drops caused by the magnitude of the drag force. The fastest growing wavelength for the RT instabilities is given by,

$$\Lambda_{RT} = 2\pi \sqrt{\frac{3\sigma}{a(\rho_l - \rho_g)}} \tag{4}$$

where σ is the drop surface tension, a is the deceleration of the drop and ρ_l and ρ_g are the liquid and gas densities, respectively. If the scaled wavelength given by,

$$\Lambda_{RT} . C_{RT} \tag{5}$$

is calculated to be smaller than the droplet diameter; RT waves are assumed to be growing on the surface of the drop. When the RT waves have been growing for a sufficient time given by,

$$C_I / \Omega_{RT} \tag{6}$$

the drop is broken up according to the RT mechanism. C_{RT} is the RT model size constant, C_I is the RT breakup time constant, and Ω_{RT} is the wavelength growth rate. More details about the KH-RT model setup will be shown later. In addition, appropriate sub-models for droplet turbulence dispersion (O'Rourke model [25]) and collision (NTC collision model [26]) are included.

Phase change due to evaporation is modeled using Frossling correlation [27]. The model developed by Price et al. [28] is also adopted which is important for flash boiling cases. Particular attention is paid to the latter phenomena, easily experienced with ammonia at relatively low ambient pressures. Here, the rate of change of the drop mass is the sum of the subcooled term M_{sc} and the superheat term M_{sh}. The subcooled term is calculated as

$$\frac{dM_{sc}}{dt} = 2\pi R_d P_\infty \frac{Sh \, D_i}{T_f \, R_f} \ln\left(\frac{P_\infty - P_v}{P_\infty - P_s}\right) \tag{7}$$

where R_d is the drop radius, P_∞ is the cell pressure, Sh is the Sherwood number, D_i is the binary diffusivity, T_f is the vapor film temperature, R_f is the vapor film specific gas constant, P_v is the partial vapor pressure of the drop species, and P_s is the saturation pressure of the species. The superheat term is given by,

$$\frac{dM_{sh}}{dt} = \frac{4 \, \pi \, R_d^2 \, \alpha \, (T - T_b)}{H_L} \tag{8}$$

where H_L is the latent heat of the liquid and T_b is the boiling temperature. The heat transfer coefficient α is obtained from the empirical relation from Adachi et al. [29]. The vapor mass diffusivity is modeled using the following equation,

$$\rho_{gas} D = 1.293 \, D_0 (T_{gas}/273)^{n_0 - 1} \tag{9}$$

where $D_0 = 2.8 \, e^{-5}$ and $n_0 = 2.75$ are properly representative values for ammonia. All other relevant liquid ammonia properties are tabulated as a function of liquid temperature.

In this work only the CFD results of 2 conditions are presented: chamber pressures set at 2 bar (flashing) and 15 bar (non-flashing), with liquid ammonia and air temperature at 293 K. An important aspect in specifying the boundary conditions for each jet is assigning the orientation and the near-exit cone angle. In the current work, plume directions are maintained the same for both flashing and non-flashing cases. Values are prescribed individually for each hole, according to the geometric model shown in Fig. 4.b. On the other hand, the chosen jet cone angle value is 25 degrees for the flashing case, and 20 degrees for the non-flashing one. This

approach, which does not attempt to change the initial jet directions when spray collapse occur under flashing conditions, is suggested by near-nozzle closeup views of flashing vs. non-flashing sprays, as for example reported by Moulai et al. in [30].

Lastly, turbulence is modeled using RANS approach with standard k-ε model with the modified constant $C_{\varepsilon 1} = 1.55$. The definition of the best setup is obtained after a parametric exploration that will be shown in the next paragraphs.
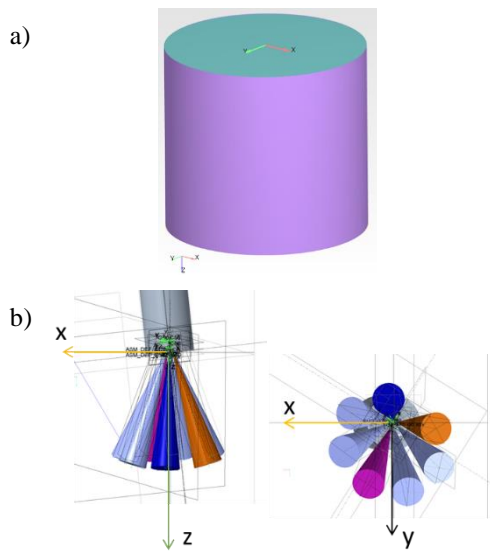

Fig. 4. Computational domain (a), spray geometry details (b).

Results and Discussion

CFD Model Parameters Exploration

In this section, the simulation results regarding the parametric exploration of the main CFD model parameters are shown. These include mesh resolution, turbulence model and jet cone angle. These explorations are presented for the flash boiling case, i.e., the 2 bar ambient pressure condition. The objective is the definition of an optimal setting, using two experimental global parameters as reference, namely, tip penetration and jet morphology.

Grid size effect

A mesh sensitivity study is performed using three different grid sizes (as shown in Table 2). This exploration is carried out prescribing a jet cone angle value of 25 degrees and using the modified Standard k-ε model, since their effects will be shown in the following sub-sections.

All the numerical curves have been evaluated considering 99% of liquid fuel mass fraction for calculating the liquid penetration, and 0.1% of vapor fuel mass fraction to calculate the vapor penetration.

Table 2. Grid parameters.

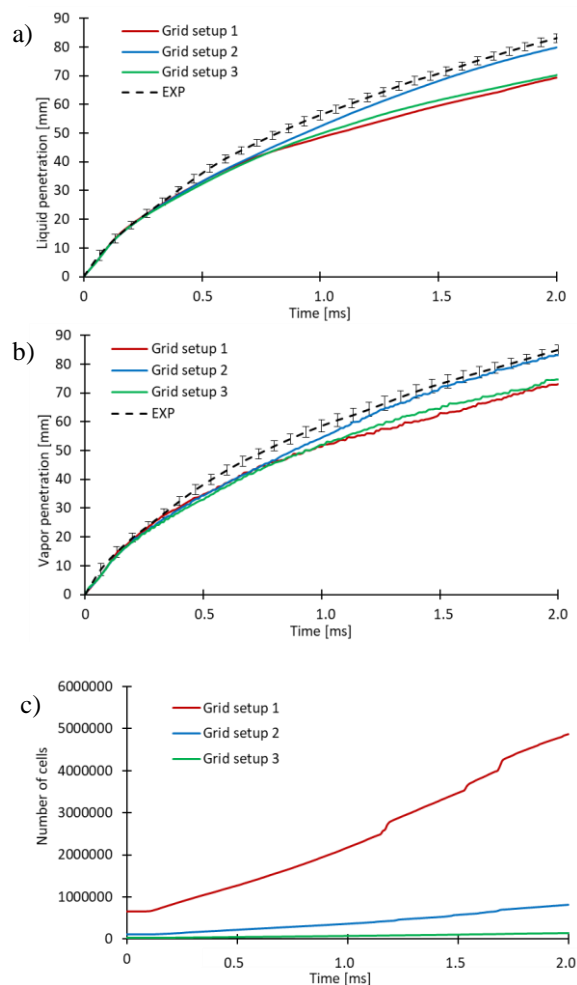|	Grid setup 1 (fine)	Grid setup 2 (intermediate)	Grid setup 3 (coarse)
Base grid size [mm]	4.0	4.0	4.0
Minimum grid size near the injector tip [mm]	0.125	0.25	0.5
Grid size in the far field region (obtained with AMR) [mm]	0.25	0.5	1.0
Maximum cell count [-]	0.3 M	1.8 M	6.0 M
Computational cost [core-h]	30	140	600

Fig. 5. Grid size effect: liquid penetration (a) vapor penetration (b), and number of computational cells (c). P_{amb} = 2 bar, T_{amb} = 293 K (modified STD k-ε, jet cone angle = 25°).

In Fig. 5, modeling results are compared with the experimental data in terms of liquid (Fig. 5.a) and vapor (Fig. 5.b) penetration: results of grid setup 1 are shown in red, grid setup 2 in blue, grid setup 3 in green, and experimental data are displayed in black. Moreover, the number of computational cells is shown in Fig. 5.c. There is no difference in penetrations up to 0.7 ms after the start of injection (ASOI), while immediately afterwards the curves begin to separate from each other. In particular, the grid setup 1 (fine) and 3 (coarse) generate a very short spray, while the grid setup 2 (intermediate) produces a penetration similar to the experiments.

Table 3 shows the grid size effect on the spray morphology obtained for the liquid phase, at 1 ms ASOI. From the numerical point of view, the droplet dimension is scaled with the droplet diameter, and also a grayscale is used. This type of visualization is meant only to produce a spray image which is visually comparable to the experimental liquid phase images, which are obtained using high speed Schlieren. The spray morphology is similar for all grid setups. Considering these results, it was decided to use for all subsequent analyses the grid setup 2, which showed better penetration accuracy and adequate morphology, with a considerable saving of computational time.

Table 3. Grid size effect on the spray morphology. $P_{amb} = 2$ bar, $T_{amb} = 293$ K (modified STD k-ε, jet cone angle = 25°).
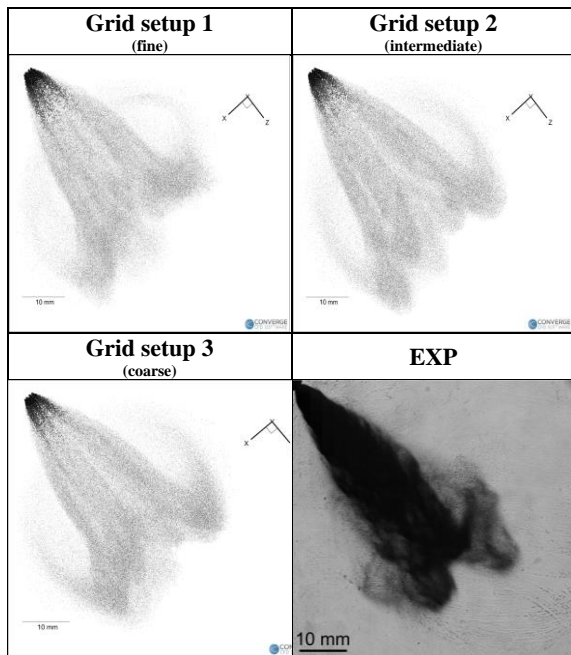
Turbulence model effect
Fig. **6** shows the results of exploring the turbulence model effect, particularly using the RNG k-ε model (blue curve), the Standard k-ε model (red curve),

and the Standard k-ε model with the modified constant $C_{ε1} = 1.55$ (green curve). The value of the constant $C_{ε1}$ is in line with the proposed round-jet correction of Pope [31], which in the case of Lagrangian sprays usually takes a slightly lower value [32,33]. This exploration is carried out prescribing a jet cone angle value of 25 degrees, whose effect will be shown in the next section. The penetrations, both liquid and vapor, calculated by the Standard k-ε model are the shorter one, while those with the RNG k-ε model are intermediates. The modification to the Standard k-ε model produces an increase in the penetration, and it can reproduce adequately well the liquid and vapor penetration measurements. Results in Table 4 show the turbulence model effect on the spray morphology based the liquid phase, at 1 ms ASOI. The spray morphology is not affected by the turbulence model. Based on the above observations, the modified Standard k-ε model has been selected.
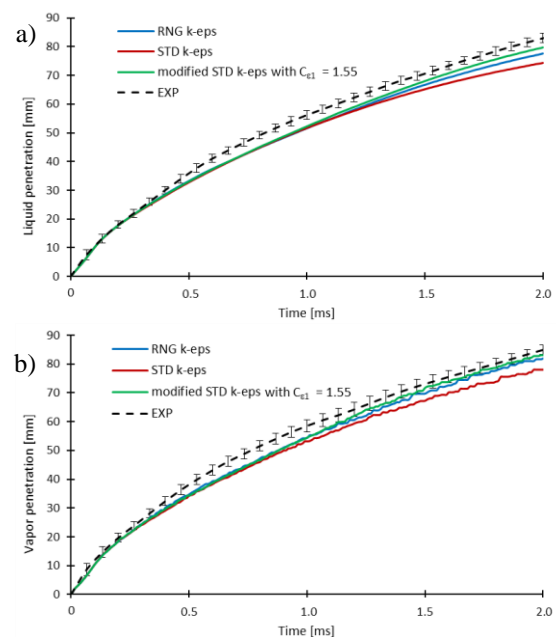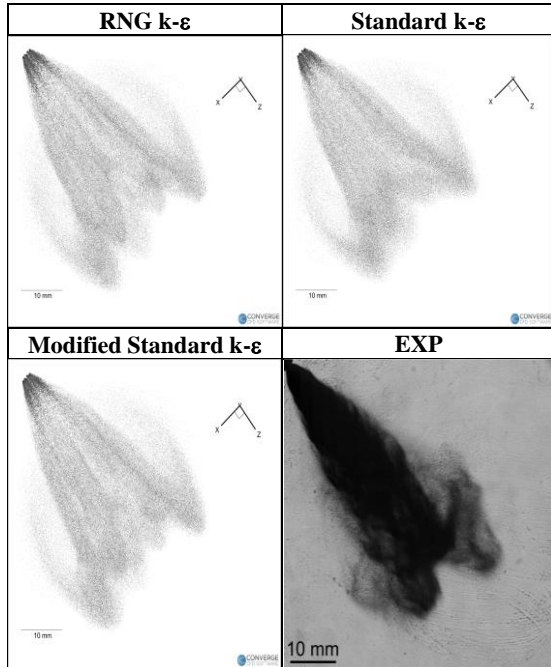

Fig. 6. Turbulence model effect: liquid penetration (a) and vapor penetration (b). $P_{amb} = 2$ bar, $T_{amb} = 293$ K (jet cone angle = 25°, intermediate grid).

Jet cone angle effect
The jet cone angle is the most influential parameter on the spray penetration and on the spray morphology. In Fig. 7, five different cone angle values are compared. The predicted liquid penetration increases as the cone angle decreases: the penetrations with cone angle values of 30 degrees (grey curve) is shorter than the experiments, while the penetrations with cone angle values of 15 degrees (red curve) and 10 degrees (blue curve) are longer than the experiments. Cone angle values of 20 and 25 degrees (yellow and green curves)

perfectly reproduce the experimental penetration (black curve).

Table 4. Turbulence model effect on the spray morphology. P_{amb} = 2 bar, T_{amb} = 293 K (jet cone angle = 25°, intermediate grid).

The spray morphology changes considerably as the cone angle varies (as shown in Table 5), because this parameter not only affects the penetration, but also the collapse of the jets.
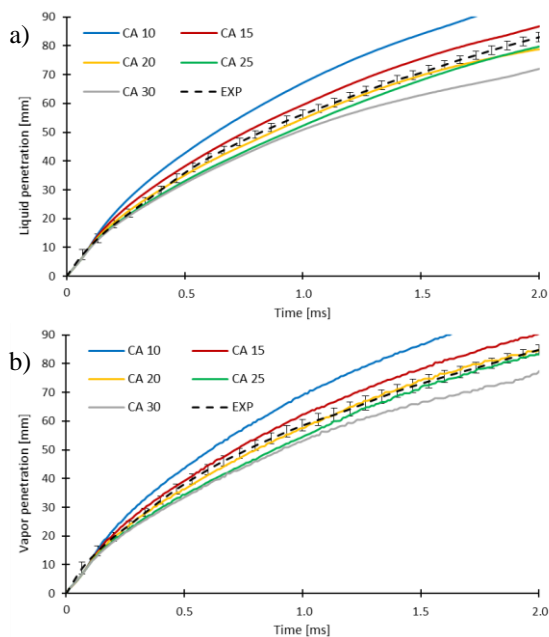

Fig. 7. Jet cone angle effect: liquid penetration (a) and vapor penetration (b). P_{amb} = 2 bar, T_{amb} = 293 K (modified STD k-ε, intermediate grid).

In particular, using cone angle values of 10 and 15 degrees, the jets are completely separated. Jets start to collapse using cone angle values bigger than 20 degrees, because this value starts producing plume-to-plume interaction. Considering the penetration comparison previously presented which suggests the range 20-25 degrees, the value of 25 has been finally selected since it reproduces in a better way the jet interaction and the experimental spray morphology. It is worth noticing that a value of 30 degrees would have further improved the visual comparison with more adequate plume collapse in the far field, but at the cost of worsening the tip penetration.

Table 5. Jet cone angle effect on the spray morphology. P_{amb} = 2 bar, T_{amb} = 293 K (modified STD k-ε, intermediate grid).
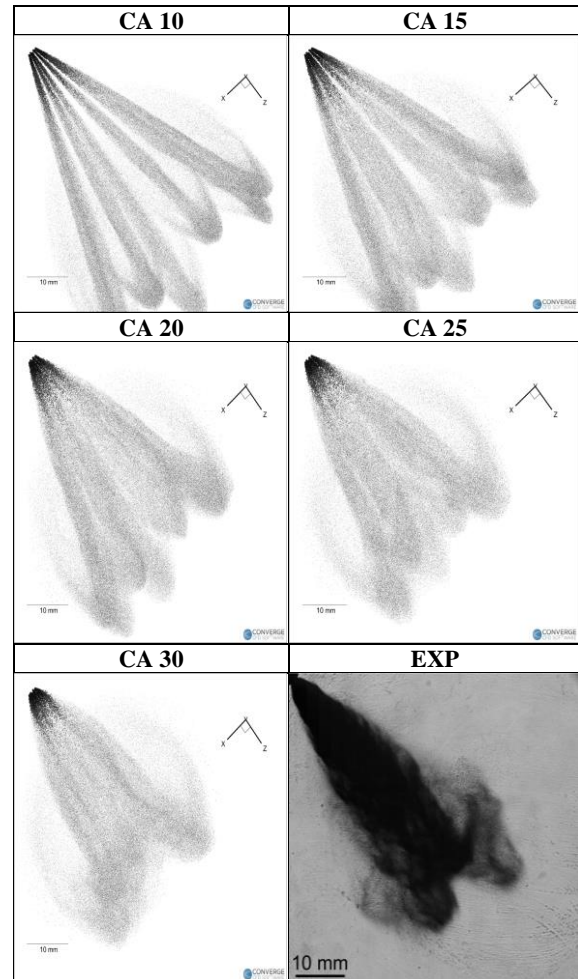
Flashing conditions: P_{amb} = 2 bar, T_{amb} = 293 K
To summarize the flash boiling case at 2 bar ambient pressure, the simulation results obtained using the optimized CFD setup are compared with the experimental results. Table 6 summarizes the KH-RT model setup for flash boiling conditions, after a preliminary exploration of KH-RT constants. It must be noted that similar values are commonly used for

conventional fuels (e.g. gasoline), under flashing conditions [34].

Table 6. KH-RT model setup for flashing ammonia spray.

KH model	Model size constant B_0 (eq. 1)	0.6
	Model breakup time constant B_1 (eq. 3)	7.0
RT model	Model size constant C_{RT} (eq. 5)	0.1
	Model breakup time constant C_I (eq. 6)	0.25

A comparison between liquid (solid lines) and vapor (dotted lines) penetration is shown in Fig. 8.a, experimental results in black, CFD results in red. Fig. **8**.b shows a comparison of the spray morphology at 1 ms ASOI. Numerical results reproduce perfectly experimental trends since the model is properly calibrated for this purpose.

Furthermore, in Fig. 9, a comparison of the local SMD is shown (experimental data in black, CFD results in red). Experimental data are useful to calibrate and optimize the model. Numerical results slightly overestimate the data measured close to the injector tip (pos. 0, 1 and 4), while the trend is well reproduced since larger SMD values in positions located in the far periphery of the jet (pos. 2 and 3) are predicted. Therefore, it can be concluded that for the flashing case, local SMD is reproduced in a

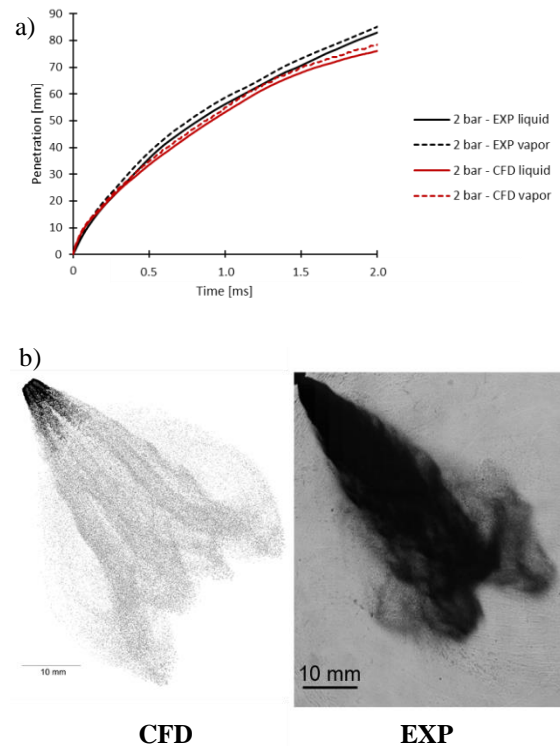satisfactorily manner using values of KH-RT model shown in Table 6.

Fig. 8. Comparison between experiments and simulation in terms of penetration (a) and spray morphology (b) for flashing ammonia spray.
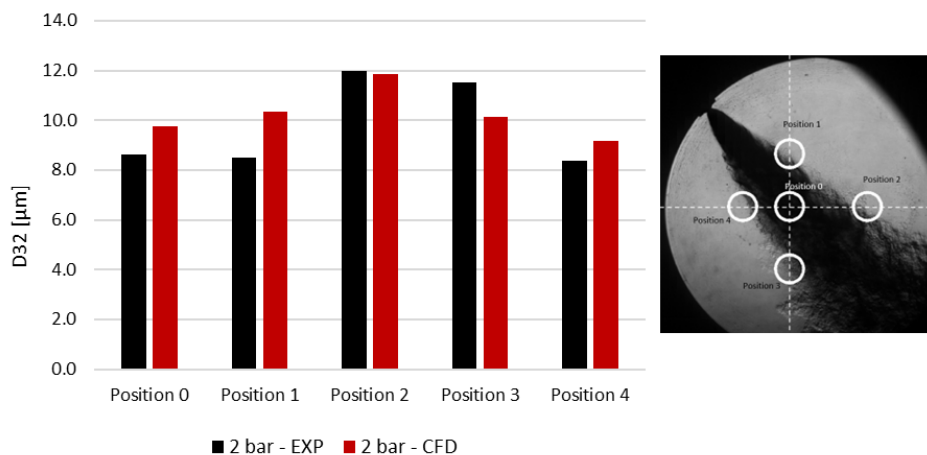

Fig. 9. SMD comparison for the different measured chamber positions - flashing ammonia spray.

Non-flashing conditions: $P_{amb} = 15$ bar, $T_{amb} = 293$ K

Moving from the flashing to the non-flashing case, it is expected that the CFD setup needs to be re-adjusted to reproduce the experimental data in the best possible way. However, to assess the robustness and predictivity of the KH-RT model, the same setup as that used for the flashing regime is also tested, but applying a reduced jet cone angle of 20

degrees [30] with same plume directions. Results in terms of local SMD in the five analyzed positions are shown in Fig. 10. Blue bars display the results with the settings previously used for flash-boiling, while red bars refer to new breakup parameters specifically recalibrated for the current non-flashing case. From the comparison with the experimental data (in black) it is evident that there is a strong discrepancy with experiments if model constants are

maintained as before. Measured SMD values increase with ambient pressure, so from flashing to non-flashing case, as shown in Table 1 or by comparing black bars in Fig. 9 and in Fig. 10. On the contrary, using the same breakup settings, local SMD values predicted by the CFD simulations decrease with pressure, therefore, the predicted trend is opposite to that observed experimentally.

Therefore, the KH-RT model has been recalibrated with significant variations as shown in Table 7 in order to reproduce the experimental SMD values, while the setup for the turbulence model remained unchanged. The jet cone angle value is 20 degrees, as already mentioned. It is noted that ammonia fuel properties are quite different from those of conventional fuels, as the required constant values reported in Table 7 are largely modified compared to gasoline or hydrocarbons [35, 36]. It is inferred that KH-RT model constants that are generally used

for those liquids are not properly suitable for a molecule like ammonia, and a specific recalibration is required.

CFD results in terms of local SMD prediction in Fig. 10 are improved, since the calibrated KH-RT results (in red) are characterized by larger diameters which are closer to experimental measurements in all 5 positions.

Table 7. KH-RT model setup for non-flashing ammonia spray.

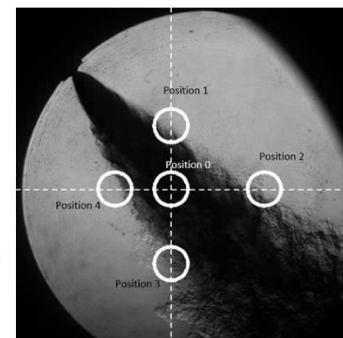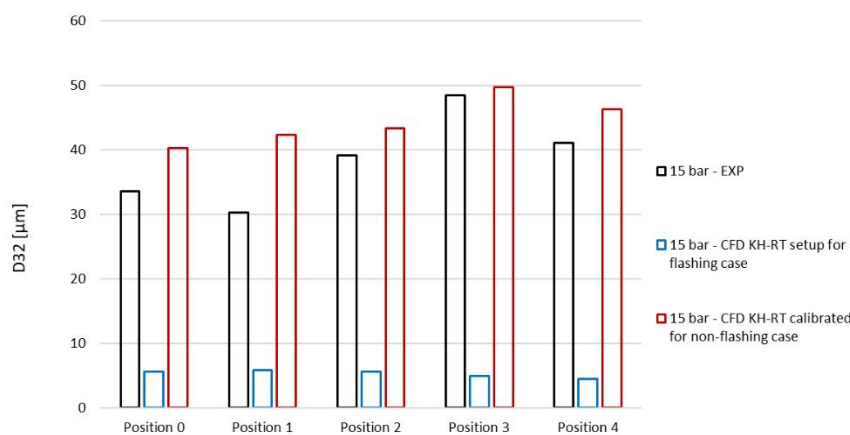| KH model	Model size constant B_0 (eq. 1)	2.0
	Model breakup time constant B_1 (eq. 3)	20.0
RT model	Model size constant C_{RT} (eq. 5)	1.0
	Model breakup time constant C_I (eq. 6)	2.5

Fig. 10. SMD comparison for the different measured chamber positions – non-flashing ammonia spray.

The same behavior is also clearly visible from the morphology of the spray shown in Table 8. Recalling that, for the numerical spray morphology images, droplet dimension is scaled with the droplet diameter, it is possible to notice that using KH-RT setup for flashing case produces a very different spray in total disagreement with the experimental evidence, with fully separate jets and very small droplets. The morphology of the spray has a marked improvement with the calibrated KH-RT setup, and the numerical shape satisfactorily reproduces the experimental one.

Lastly, the comparison in terms of liquid and vapor penetration shown in Fig. 11 shows that the effect of the breakup model on penetration is marginal, and the CFD model with calibrated KH-RT is able to reproduce both penetrations in a satisfactorily manner.

Flashing vs. Non-flashing conditions summary
As a summary, here is reported a final comparison between the results of the two cases, to better appreciate the effect of the transition between flash boiling and non-flashing regimes for ammonia sprays. The KH-RT model parameters are those specifically calibrated for each regime (see Table 6 and Table 7). The liquid (solid lines) and vapor (dotted lines) penetrations are compared in Fig. 12 against experimental spray data. The 15 bar case is characterized by a lower penetration compared to the 2 bar case due to the increased ambient density. This comparison clearly shows the good agreement between simulations and experiments in terms of liquid spray tip penetration.

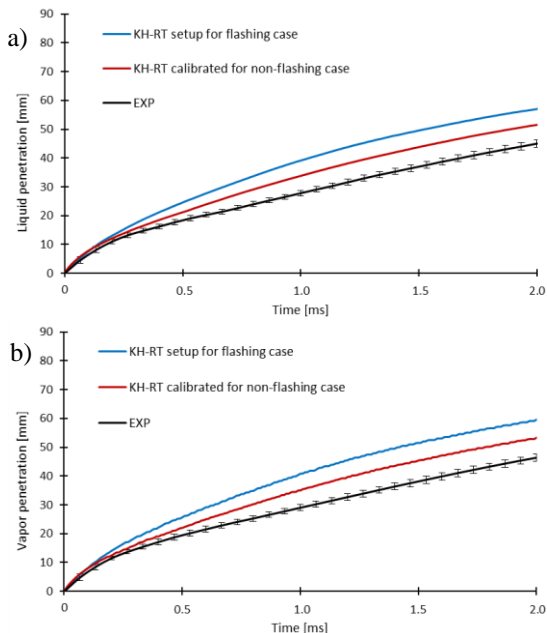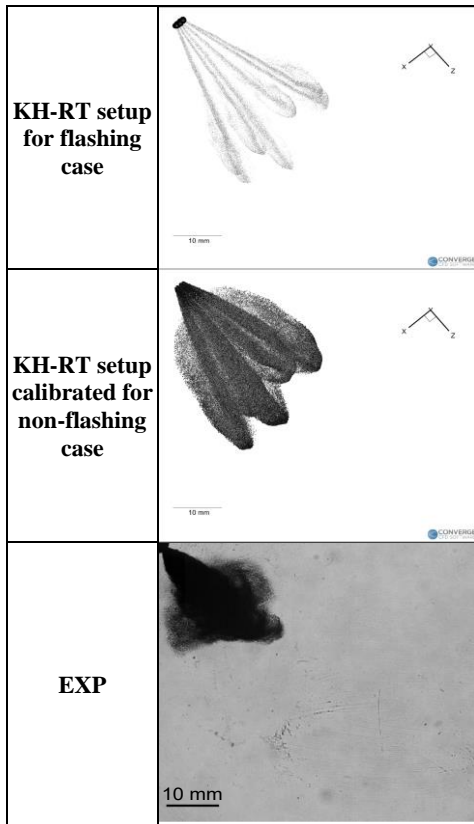**Table 8.** KH-RT effect on the spray morphology, in non-flashing conditions.

Overall, the experimental spray shape is satisfactorily reproduced in both conditions, as shown in the comparison in Table 9.
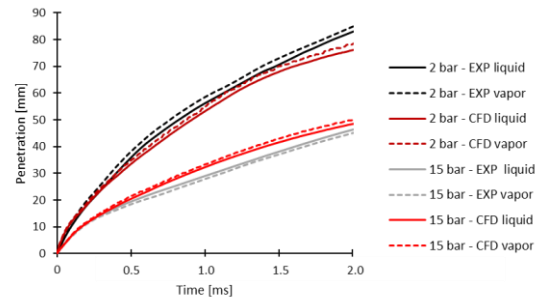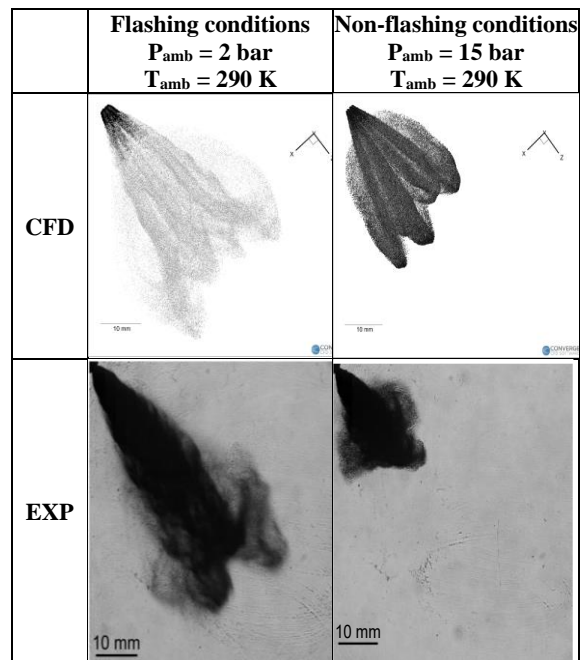

Fig. 12. Comparison between experiments and simulation in terms of liquid penetration, flashing (2 bar) vs. non-flashing (15 bar) conditions.

Table 9. Comparison between experiments and simulation in terms of spray morphology, flashing vs. non-flashing conditions.

Lastly, the SMD comparison is shown in Fig. 13, with experimental results reported in black and CFD results in red. It was necessary to adapt the coefficients of the KH-RT breakup model moving from the flash boiling regime to the non-flashing one in order to reproduce experimental SMD trends. This suggests that capturing spray local details across all the regimes with a single model is still challenging, especially with a new fuel such as ammonia. Nevertheless, analyzing the five positions, trend-wise predictions indicate larger droplets on the external locations (pos. 2 and 3), as observed in the measurements.
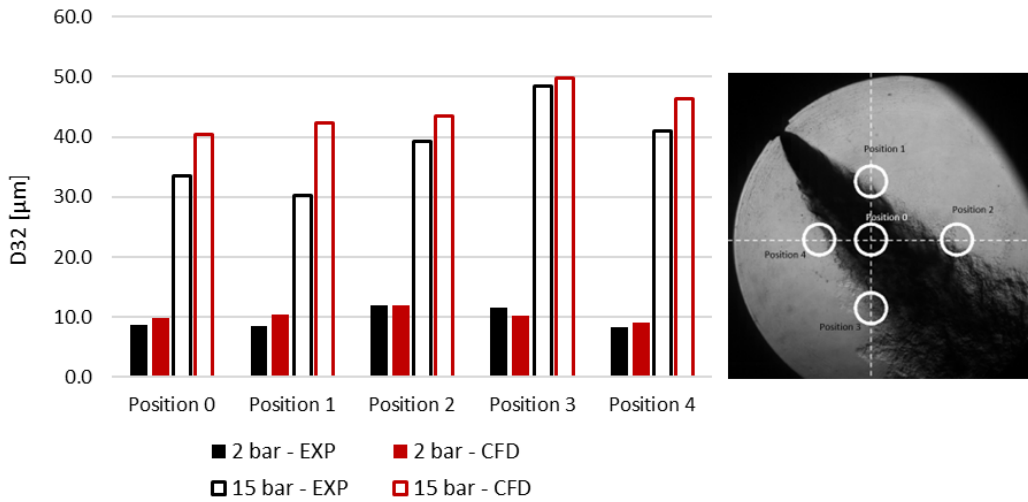

Fig. 11. KH-RT effect on the liquid penetration (a) and vapor penetration (b), in non-flashing conditions.

Fig. 13. Comparison between experiments and simulation in terms of local SMD, flashing (2 bar) vs. non-flashing (15 bar) conditions.

Using these validated CFD models for the two regimes, many additional features of ammonia sprays can be analyzed. Ammonia vapor mass and local gas vs. liquid temperatures can be of interest.

In Table 10, a comparison between vapor ammonia mass fraction profiles at 10, 20 and 30 mm distance from the nozzle is shown, at 1 ms ASOI. For all distances, a marked difference can be noted between the flashing case and the non-flashing case: for the 2 bar case there is a high concentration of ammonia vapor which even exceeds 20% mass fraction, while for the 15 bar case the quantity of ammonia vapor is negligible since it reaches maximum values around 5%. This difference in ammonia vapor behavior is due to the different regimes analyzed. Basically, ammonia vapor is created due to flash boiling phenomenon, and this is the reason for being present in a greater amount for the 2 bar case. In addition, there is another characteristic effect of flash boiling, the collapse of the jet, visible in particular for the external jets whose imprints are merged.
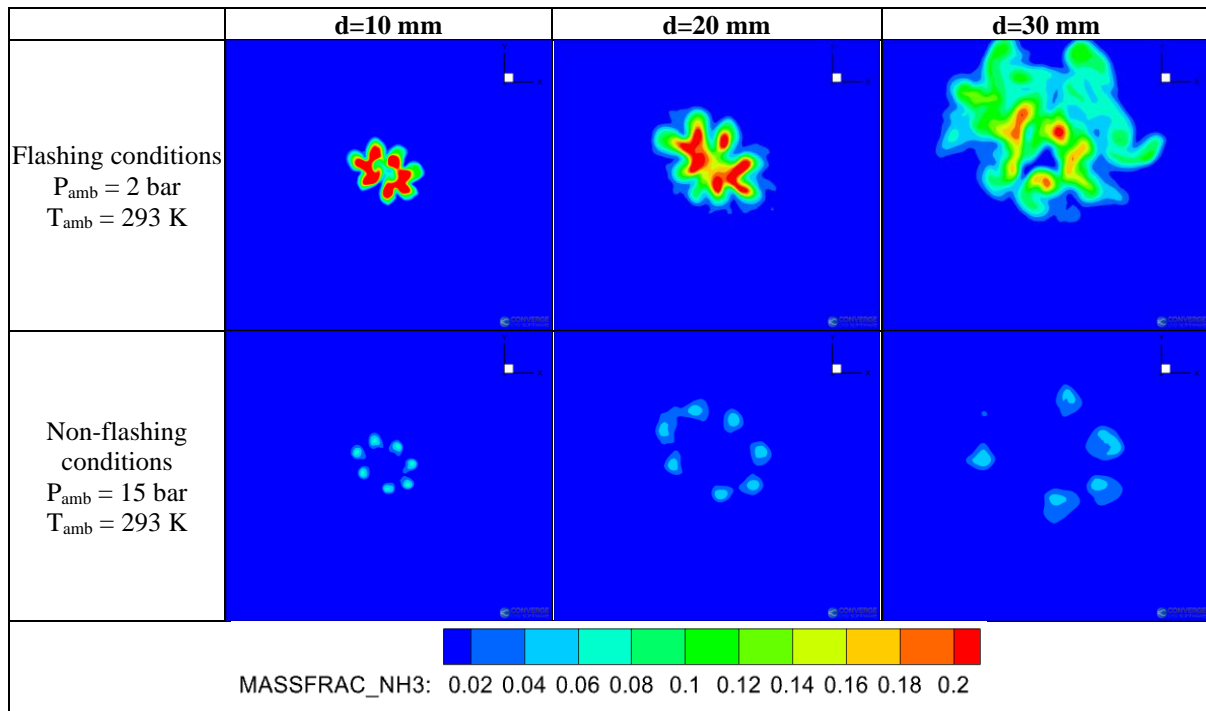

Table 10. Comparison between vapor ammonia mass fraction at 10, 20 and 30 mm distance from the injector position, at 1 ms ASOI, in the color range between 0 and 0.2.

Images in Table 11 show a comparison of the droplet and gas temperatures for the 2 cases analyzed, at 1 ms ASOI: the droplet and gas temperatures are displayed in the range between 220 and 290 K, noting that the gas temperature is represented in a slice passing through the injector axis. The initial temperature of the chamber is 293 K, and also the liquid ammonia is injected at 293 K.

It is also worth recalling that ammonia has a large heat of vaporization compared to hydrocarbon fuels. As an example, at 293 K ammonia heat of vaporization is 1187 kJ/kgK, while iso-octane has a value of 310 kJ/kgK. As a consequence, a strong cooling effects is observed with ammonia, especially under flash-boiling conditions. The predicted temperatures have distinct features for the two regimes,

- Under non-flashing conditions, droplets are in the subcooled regime at 15 bar. Vaporization causes the particles to cool down to about 270 K, while the surrounding gas cools by a few degrees, from 293 K down to about 285 K. The cooling effect is mild, but considering that liquid and gas are introduced at room temperature, the effects is not negligible.

- For the 2 bar case, flash boiling causes a strong thermal imbalance due to the rapid phase change of liquid ammonia to vapor. The droplets reach temperatures of 220 K a few millimeters after the injection point, and correspondingly the temperature of the surrounding gas cools down by about 30 K with respect to the initial condition, to about 260 K. This can be interpreted taking into account that ammonia saturation temperature at 2 bar is 255 K, so at equilibrium the liquid and the surrounding vapor tend towards this temperature. In addition to that, local dynamics play a role. Local pressure can go below the average ambient level, and the fast process can also lead to a certain degree of subcooling during the phase change, with undershooting below its equilibrium saturation temperature. These aspects can justify the low temperature levels recorded locally for the liquid ammonia.

It is here acknowledged that these predicted temperature values will require more extensive investigation to be validated, but still provide important insights into ammonia phase change in flashing and non-flashing regimes.

1

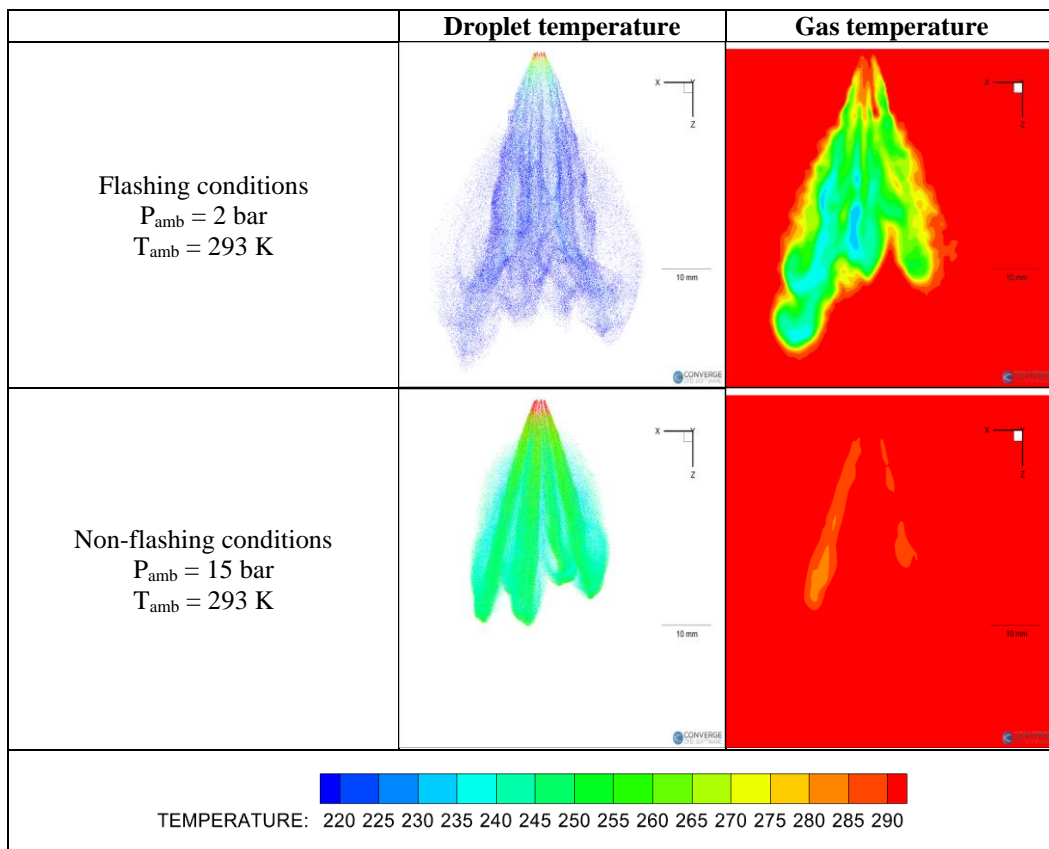|	Droplet temperature	Gas temperature
Flashing conditions P_{amb} = 2 bar T_{amb} = 293 K		
Non-flashing conditions P_{amb} = 15 bar T_{amb} = 293 K		
TEMPERATURE: 220 225 230 235 240 245 250 255 260 265 270 275 280 285 290		

Table 11. Comparison between droplet and gas temperature, at 1 ms ASOI.

Conclusions

In this work, results of CFD simulations of ammonia sprays and the comparison with experimental data are presented. Two different conditions are explored in order to compare flash boiling and non-flashing regimes.

- A predictive calibrated CFD setup within the CONVERGE v3.0 CFD software package is defined for ammonia spray through a parametric calibration of grid resolution, turbulence model, prescribed jet cone angle and breakup model constants.
- Global spray parameters such as liquid and vapor tip penetration and spray morphology are relatively easy to reproduce, while local features and atomization levels will require further theoretical development for calibration-free models.
- Capturing spray local details (such as SMD) across all the regimes with a single model or setup is still challenging, especially with a new fuel such as ammonia.
- The trends in droplet and gas temperatures predicted by the CFD highlight the strong cooling effects also due to the large heat of vaporization, even if predicted values require more in-depth investigations and data for validation.

Future works will include the exploration of additional operating conditions for a full assessment of the flash boiling phenomenon of ammonia sprays.

Nomenclature

ASOI	After Start of Injection
CFD	Computational Fluid Dynamics
GDI	Gasoline Direct Injector
KH	Kelvin-Helmholtz
RT	Rayleigh-Taylor
SMD	Sauter-Mean-Diameter
RANS	Reynolds-Averaged Navier-Stokes

Acknowledgments

Conflicts of Interest

The authors declare no conflict of interest. The funders had no role in the design of the study; in the collection, analyses, or interpretation of data; in the writing of the manuscript, or in the decision to publish the results.

References

1. Sacramento E.M., Carvalho P., Lima L.C., Veziroglu T. Feasibility study for the transition towards a hydrogen economy: A case study in Brazil. *Energy Policy* 2013, 62, 3–9; doi: https://doi.org/10.1016/j.enpol.2013.06.071.

2. Li Y., Bi M., Li B., Zhou Y., Huang L., Gao W. Explosion hazard evaluation of renewable hydrogen/ammonia/air fuels. *Energy* 2018, 159, 252–263; doi: https://doi.org/10.1016/j.energy.2018.06.174.

3. Dimitriou P., Javaid R. A review of ammonia as a compression ignition engine fuel. *Int. J. Hydrogen Energy* 2020, 45, 7098–7118; doi: https://doi.org/10.1016/j.ijhydene.2019.12.209.

4. Valera-Medina A., Xiao H., Owen-Jones M., David W.I.F., Bowen P.J. Ammonia for power. *Prog. Energy Combust. Sci.* 2018, 69, 63–102; doi: https://doi.org/10.1016/j.pecs.2018.07.001.

5. Valera-Medina A., et al. Review on Ammonia as a Potential Fuel: From Synthesis to Economics. *Energy Fuels* 2021, 35, 6964–7029; doi: https://doi.org/10.1021/acs.energyfuels.0c03685.

6. Wijayanta A.T., Oda T., Purnomo C.W., Kashiwagi T., Aziz M. Liquid hydrogen, methylcyclohexane, and ammonia as potential hydrogen storage: Comparison review. *Int. J. Hydrogen Energy* 2019, 44, 15026–15044; doi: https://doi.org/10.1016/j.ijhydene.2019.04.112.

7. Rehbein M.C., Meier C., Eilts P., Scholl S. Mixtures of Ammonia and Organic Solvents as Alternative Fuel for Internal Combustion Engines. *Energy Fuels* 2019, 33, 10331–10342; doi: https://doi.org/10.1021/acs.energyfuels.9b01450.

8. Montanaro A., Allocca L. Study of Liquid and Vapor Phases of a GDI Spray, Combust. Sci. Technol. 2019, 191: 1600–1608; doi: https://doi.org/10.1080/00102202.2019.1594796.

9. Chang M., Park J.H., Kim H.I., Park S. Flash boiling macroscopic spray characteristics of multi-hole direct injection injectors with different hole arrangement. *Appl. Therm. Eng.* 2020, 170, 114969; https://doi.org/10.1016/j.applthermaleng.2020.114969.

10. Xu M., Zhang Y., Zeng W., Zhang G., Zhang M. Flash Boiling: Easy and Better Way to Generate Ideal Sprays than the High Injection Pressure. *SAE Int. J. Fuels Lubr.* 2013, 6, 137–148; doi: https://doi.org/10.4271/2013-01-1614.

11. Lacey J., Poursadegh F., Brear M.J., Gordon R., Petersen P., Lakey C., Butcher B., Ryan S.

Generalizing the behavior of flash-boiling, plume interaction and spray collapse for multi-hole, direct injection. *Fuel* 2017, 200, 345–356; doi: https://doi.org/10.1016/j.fuel.2017.03.057.

12. Chang M., Lee Z., Park S., Park S. Characteristics of flash boiling and its effects on spray behavior in gasoline direct injection injectors: A review. *Fuel* 2020, 271, 117600; doi: https://doi.org/10.1016/j.fuel.2020.117600.

13. Wang L., Wang F., Fang T. Flash boiling hollow cone spray from a GDI injector under different conditions. *Int. J. Multiph. Flow* 2019, 118, 50–63; https://doi.org/10.1016/j.ijmultiphaseflow.2019.05.009.

14. Pelé R., Mounaïm-Rousselle C., Bréquigny P., Hespel C., Bellettre J., et al. First Study on Ammonia Spray Characteristics with a Current GDI Engine Injector. *Fuels* 2021; 2:253–71; doi: https://doi.org/10.3390/fuels2030015.

15. Shiyan L., Li T., Wang N., Zhou X., Chen R., and Yi P. An investigation on near-field and far-field characteristics of superheated ammonia spray. *Fuel* 2022, 324: 124683; doi: https://doi.org/10.1016/j.fuel.2022.124683.

16. Qiang C., Ojanen K., Diao Y., Kaario O., and Larmi M. Dynamics of the Ammonia Spray Using High-Speed Schlieren Imaging. *SAE Technical Papers* 2022, 2022-01-0053; doi: https://doi.org/10.4271/2022-01-0053.

17. Scharl V., Lackovic T., Sattelmayer T. Characterization of ammonia spray combustion and mixture formation under high-pressure, direct injection conditions, *Fuel* 2023, 333(2): 126454; doi: https://doi.org/10.1016/j.fuel.2022.126454.

18. Jessica G., Netzer C., Lewandowski M.T., and Løvås T. Modelling of liquid injection of ammonia in a direct injector using Reynolds-averaged Navier–Stokes simulation. *Scandinavian Simulation Society* 2022: 405-412.

19. Pandal A., Battistoni M., Zembi J., et al. GDI Ammonia Spray Numerical Simulation by means of OpenFOAM, *SAE Technical Paper* 2023-01-0311, (2023); doi: https://doi.org/10.4271/2023-01-0311

20. Nilaphai O., Hespel C., Chanchaona S., Mounaïm-Rousselle C., ILASS–Asia 2017 Oct. 18-21, 2017, Jeju, Korea Spray (2017) Oct. 18-21.

21. Richards K.J., Senecal P.K., and Pomraning E., "CONVERGE v.3.0 Documentation," Convergent Sciences Inc., 2020.

22. Senecal P., Richards K., Pomraning E., Yang T. et al. A New Parallel Cut-Cell Cartesian CFD Code for Rapid Grid Generation Applied to in-Cylinder Diesel Engine Simulations, *SAE Technical Paper* 2007, 2007-01-0159, doi: https://doi.org/10.4271/2007-01-0159.

23. Issa R.I. Solution of the Implicitly Discretised Fluid Flow Equations by Operator-Splitting, *J Comp Phys* 1986, 62(1): 40-65; doi: https://doi.org/10.1016/0021-9991(86)90099-9.

24. Senecal P. K., Pomraning E., Richards K. J, Som S., Grid-Convergent Spray Models for Internal Combustion Engine Computational Fluid Dynamics Simulations. *ASME J Energy Res Tech*. 2014, Vol. 136 / 012204-1; doi: https://doi.org/10.1115/1.4024861.

25. O'Rourke P.J. Collective Drop Effects on Vaporizing Liquid Sprays, Ph.D. Thesis, Princeton University, Princeton, NJ, United States, 1981.

26. Schmidt D.P. and Rutland C.J. A New Droplet Collision Algorithm, *J Comp Phys*. 2000, 164(1): 62-80; doi: https://doi.org/10.1006/jcph.2000.6568.

27. Frössling N. Über die Verdunstung fallender Tropfen Gerlands Beitrag zur Geophysik 1938, 52:170-216

28. Price C., Hamzehloo A., Aleiferis P., and Richardson R. An Approach to Modeling Flash-Boiling Fuel Sprays for Direct-Injection Spark-Ignition Engines, *Atomization Sprays* 2016, 26(12): 1197-1239. doi: https://doi.org/10.1615/AtomizSpr.2016015807.

29. Adachi M., Tanaka D., Hojyo Y., Al-Roub M., Senda J., and Fujimoto H. Measurement of fuel vapor concentration in flash boiling spray by infrared extinction/scattering technique, *JSAE Review* 1996, 17:231-237. doi: https://doi.org/10.1016/0389-4304(96)00025-2.

30. Moulai M., Grover R., Parrish S., and Schmidt D. Internal and Near-Nozzle Flow in a Multi-Hole Gasoline Injector Under Flashing and Non-Flashing Conditions, *SAE Technical Paper* 2015, 2015-01-0944; doi: https://doi.org/10.4271/2015-01-0944.

31. Pope S. An explanation of the turbulent jet/plane jet anomaly. *AIAA* 1978, 16: 279-281; doi: https://doi.org/10.2514/3.7521

32. Desantes J. M., Garcia-Oliver J. M., Pastor J. M., Pandal A. A comparison of Diesel Sprays CFD modeling approaches: DDM versus Σ-Y Atomization model. *Atomization Sprays*. 2016, 26 (7): 713-737; doi: https://doi.org/10.1615/AtomizSpr.2015013285.

33. Paredi D, Lucchini T, D'Errico G, Onorati A, Pickett L, Lacey J. Validation of a comprehensive computational fluid dynamics methodology to predict the direct injection process of gasoline sprays using Spray G experimental data. *Int J Engine Res*. 2020, 21(1):199-216. doi: https://doi.org/10.1177/1468087419868020.

34. Duronio F., De Vita A., Allocca, L., Montanaro, A. et al., "CFD Numerical Reconstruction of the Flash Boiling Gasoline Spray Morphology," *SAE Technical Paper* 2020, 2020-24-0010; doi: https://doi.org/10.4271/2020-24-0010.

35. Paredi D., Lucchini T., D'Errico G., Onorati A. et al. Combined Experimental and Numerical Investigation of the ECN Spray G under Different

Engine-Like Conditions, *SAE Technical Paper* 2018, 2018-01-0281; doi: https://doi.org/10.4271/2018-01-0281.

36. Sciortino D.D., Bonatesta F., Hopkins E., Bell D., Cary M. A systematic approach to calibrate spray and break-up models for the simulation of high-pressure fuel injections. *Int J Engine Res*. 2021, 24(2); doi: https://doi.org/10.1177/14680874211050787